Nature Communications

https://doi.org/10.1038/s41467-025-67085-w

Article in Press

K isotopes trace temporal silicate weathering intensity

Received: 30 April 2025

Accepted: 21 November 2025

Cite this article as: Gou, L.-F., Sun, H., Gu, H.-O. *et al.* K isotopes trace temporal silicate weathering intensity. *Nat Commun* (2025). https://doi.org/10.1038/s41467-025-67085-w

Long-Fei Gou, He Sun, Hai-Ou Gu, Philip A. E. Pogge von Strandmann, Wenshuai Li, David J. Wilson, Jun Xiao, Zhi-Qi Zhao, Albert Galy & Zhangdong Jin

K isotopes trace temporal silicate weathering intensity

Long-Fei Gou[1,2,3*], He Sun[4], Hai-Ou Gu[4], Philip A.E. Pogge von Strandmann[5], Wenshuai Li[6], David J. Wilson[7], Jun Xiao[2], Zhi-Qi Zhao[1], Albert Galy[3], Zhangdong Jin[2,1*]

1 State Key Laboratory of Loess Science, Department of Geography, Chang'an University, Xi'an, 710054, China;

2 State Key Laboratory of Loess Science, Institute of Earth Environment, Chinese Academy of Sciences, Xi'an 710061, China;

3 Centre de Recherches Pétrographiques et Géochimiques, UMR7358, CNRS, Université de Lorraine, 54500 Vandoeuvre les Nancy, France;

4 School of Resources and Environmental Engineering, Hefei University of Technology, 230009, Hefei, China;

5 Mainz Isotope and Geochemistry Centre (MIGHTY), Institute of Geosciences, Johannes Gutenberg-Universitat Mainz, 55128 Mainz, Germany;

6 School of Earth Sciences, China University of Geosciences, Wuhan 430074, China;

7 London Geochemistry and Isotope Centre (LOGIC), Department of Earth Sciences, University College London, Gower Street, London WC1E 6BT, UK.

Corresponding Authors: Long-Fei Gou (lfgou@chd.edu.cn); Zhangdong Jin (zhdjin@ieecas.cn)

Abstract: Silicate weathering alters the biogeochemical compositions of the lithosphere, hydrosphere, and atmosphere, and thereby regulates both nutrient cycling and habitable temperatures on Earth, but tracing silicate weathering effectively remains a challenge. Potassium (K) isotopes have been proposed as a tracer of silicate weathering intensity spatially, but there is a significant gap in how and why K isotopes trace silicate weathering temporally. Here we investigate seasonal variations in dissolved K isotopes in the middle Yellow River, which drains a large area of homogeneous loess that represents the average geochemical composition of the upper continental crust, and experiences significant climatic seasonality driven by the East Asian monsoon. We find that K isotopes show strong seasonality as a function of aluminosilicate neoformation following silicate dissolution, and thus could serve as a tracer of silicate weathering intensity. We derive an empirical relationship of $\delta^{41}K_{rw} = -0.07 \times \ln(W/D) - 0.38$, where W(silicate chemical weathering)/D(denudation) refers to silicate weathering intensity.

Key words: K isotopes, Silicate weathering intensity, Seasonality, the Yellow River, Chinese Loess Plateau (CLP)

INTRODUCTION

Silicate weathering alters the biogeochemical compositions of the lithosphere, hydrosphere, and atmosphere, and stabilizes Earth's habitability by regulating atmospheric CO_2 concentrations over geological timescales[1-3]. However, the factors controlling silicate weathering remain unclear, especially in deep time, with a standing debate on the relative roles of tectonic uplift[4] and climate change[3, 5, 6]. Such questions could be better addressed through the development of new tracers of silicate weathering that can be applied in both the modern day and the geological past.

Potassium (K) is almost exclusively hosted in silicates[7-9] and has two stable isotopes, ^{39}K and ^{41}K, which are proposed to fractionate during dissolution, adsorption and incorporation[7, 10, 11]. As such, K isotopes ($\delta^{41}K$) are a promising tracer of chemical weathering intensity (the ratio of chemical weathering and total denudation flux)[7-12]. For example, a weak relationship between the annually-averaged chemical weathering intensity and $\delta^{41}K$ values in river waters ($\delta^{41}K_{rw}$) was reported spatially at a global scale[8]. However, seasonal variations in $\delta^{41}K_{rw}$ values have not yet been demonstrated, despite the reported sensitivity of silicate weathering to climatic parameters[13-15]. If $\delta^{41}K_{rw}$ values do serve as a tracer for spatial variations in chemical weathering intensity, then we could expect them to also respond of silicate weathering to climate forcing[7-9, 16].

Here, we show how $\delta^{41}K_{rw}$ can act as a tracer for temporal variations in silicate weathering intensity under variable climatic conditions, including pronounced temperature variations and extreme hydrological events. To this end, we determine $\delta^{41}K_{rw}$ values in a (semi-)arid region with limited vegetation using high-resolution temporal sampling in the middle reaches of the Yellow River (Fig. S1). In arid environments, low vegetation cover minimizes biological uptake and thus reduces the biological effect on K isotopic fractionation. This river system drains across easily erodible and relatively homogeneous loess (Fig. S1) that closely represents the average chemical composition of the upper continental crust (UCC[17]). Pronounced seasonal climate changes due to the East Asian monsoon make the Yellow River a highly suitable setting to define the seasonal response of $\delta^{41}K_{rw}$ to climate. We find significant $\delta^{41}K_{rw}$ seasonality as a function of aluminosilicate neoformation after silicate dissolution, suggesting that it can serve as a tracer of silicate weathering intensity. We also establish an empirical relationship of $\delta^{41}K_{rw} = -0.07 \ln(W/D) - 0.38$, where W(silicate chemical weathering)/D(denudation) refers to silicate weathering intensity.

RESULTS

Seasonal variations in temperature, discharge, and physical erosion rates

During the sampling year of 2013, the water temperature continuously increased from a January minimum of 0°C to an August maximum of 29°C, and then gradually decreased (Fig. 1). The water discharge at the Longmen hydrological station was 24.5 km^3/yr in 2013. During the dry season, there were low values of water discharge in January–February, which then peaked in March, and then declined to a minimum of 152 m^3/s in May (Fig. 1). We defined the first small water discharge peak as an "ice-melting interval" because it was a result of ground snow melting from 16th March to 13th April when the air temperature was above 0°C. During the monsoon season (June to mid-September), the consistently high-water discharge (>600 m^3/s; Fig. 1) reflected the frequent, monsoon-driven precipitation within the Yellow River basin. Notably, there was a storm event from 22nd to 25th July, which resulted in a maximum water discharge of 2400 m^3/s[18-21]. After the monsoon season, the water discharge decreased gradually to relatively low values for October to December. All the waters of the middle Yellow River were alkaline with pH values between 7.05 and 8.71[21].

The Yellow River is highly sediment-laden, contributing ~10% of the global sediment input to oceans[22]. Seasonal variations in the suspended particulate matter (SPM) flux in the middle Yellow River span almost five orders of magnitude (Fig. 1). The SPM flux was low and fairly constant during the dry season, with a spike during the ice-melting interval, whereas high concentrations and fluxes of SPM characterized the monsoon season (Fig. 1). The highest concentrations and fluxes of SPM were recorded during the storm event in July. Overall, physical erosion rates (PER) during the monsoon season were one to four orders of magnitude higher than those during the dry season

(Figs. 1 and S2), suggesting that abundant loess was eroded into the river during the monsoon season[18-21].

K concentrations

The time-series of the K concentrations ([K^+]) and $\delta^{41}K_{rw}$ values of the Yellow River water are shown in Fig. 1 and Table S1. The mean [K^+] in the river waters was 110 μmol/L, ranging from 89 μmol/L for the storm event to 163 μmol/L during the winter, with significant seasonal variations. These [K^+] values fit within the range of global large rivers (7 to 180 μmol/L[7, 8]) and the Mun River in Thailand (58 to 360 μmol/L[16]). There was no correlation of [K^+] with [SO_4^{2-}], [Cl^-], or [NO_3^-]. Similar to observations from global rivers[5], the riverine K^+ flux was positively correlated with the PER in the middle Yellow River (Fig. S2).

Sequential extraction results for K from the Lingtai loess are given in Table S3, aiming to extract the salt (‘evap’, water-soluble fraction), carbonate (‘carb’, 5% acetic acid-soluble fraction), and the silicate (‘sil’, residue after sequential extraction) fractions of the loess[23, 24]. Generally, both the salt and carbonate fractions contain relatively little K, with 0.14 ± 0.12 mg/g and 0.62 ± 0.24 mg/g, respectively[23, 24]. In contrast, the silicate fraction contains K concentrations two orders of magnitude higher than those in the salts and carbonate fractions, with a mean of 18.3 ± 4.3 mg/g that is similar to the composition of the UCC (19.00 ± 2.99 mg/g[11, 17]). Given that the SPM in the middle Yellow River has the same chemical, mineralogical, and Li, Mg and Ba isotopic compositions as the loess[18-20, 25], we used 18.3 ± 4.3 mg/g of the loess as $[K]_{SPM}$[11, 17, 23].

The mean [K^+] of the rainwater samples was ~30 μmol/L (a range of 17–47 μmol/L, Table S2), while the mean rainwater K/Cl ratio of 0.33 excludes a recycled sea-salt origin, since sea-salt has a typical K/Cl ratio of 0.02 and $\delta^{41}K$ value of 0.12 ± 0.07‰[8, 26]. Therefore, the high [K^+] in the rainwater was likely related to the high dust contributions in the Asian interior[27], as similarly inferred for Li, Mg, Sr, and Ba isotopes[18-20, 27]. A sewage water sample collected in farmland had [K^+] of 827 μmol/L (Table S2), which is higher than any other samples collected in the middle Yellow River. A groundwater sample had [K^+] of 62 μmol/L (Table S2), which is higher than the rain water but slightly lower than the river waters.

K isotopes

Clear seasonality was observed in the $\delta^{41}K_{rw}$ values of the middle Yellow River water, which ranged between -0.37‰ and +0.27‰, far beyond the typical analytical 2 s.d. of 0.11‰ (Fig. 1). This finding represents the first reported example of seasonal $\delta^{41}K_{rw}$ variations, which span the overall range of $\delta^{41}K_{rw}$ variations observed globally (0.65‰), even taking spatial variations into consideration[7, 8, 16] (Fig. S3). Generally, during the dry and cold seasons, $\delta^{41}K_{rw}$ values were low (-0.37‰ to -0.10‰). In contrast, during the warm and wet monsoonal season, $\delta^{41}K_{rw}$ values were high (-0.10‰ to +0.27‰; Fig. 1). A similar pattern (though smaller magnitude) was also observed in the Yangtze River, with the wet season corresponding to high $\delta^{41}K_{rw}$ values and the dry season to low $\delta^{41}K_{rw}$ values[7].

Sequential extraction experiments on five loess samples gave $\delta^{41}K_{evap}$ = +0.03 ± 0.30‰, $\delta^{41}K_{carb}$ = -0.17 ± 0.08‰, and $\delta^{41}K_{sil}$ = -0.36 ± 0.12‰ (Table S3) [23, 24]. The $\delta^{41}K_{sil}$ values are similar to the bulk silicate earth (BSE) and the UCC ($\delta^{41}K$ of -0.48‰ to -0.35‰[11, 28]; Fig. S3). Heavy K isotopes are preferentially incorporated into K-bearing evaporites due to the equilibrium isotope effects that result from changes in coordination number, bond length, and bond strength[29, 30]. Hence, we suggest that the evaporites and carbonates in loess are mainly secondary minerals that formed after dissolution of the primary eolian loess, because higher $\delta^{41}K$ values are observed for the secondary evaporites and carbonates than for the silicates in the loess, as expected[30].

The rainwater sample had a very negative $\delta^{41}K$ value of -0.68 ± 0.13‰ (Table S2), together with K/Cl molar ratios between 0.15 and 0.48, further supporting that it was not of sea-salt origin. Given its very different composition from the $\delta^{41}K_{rw}$ and the occurrence of higher $\delta^{41}K_{rw}$ values at times of high-water discharge (Fig. 1), rainwater input is likely to be negligible. Similarly, a sewage sample collected on farmland had a $\delta^{41}K$ value of -0.50 ± 0.03‰ (Table S2), which also excludes a significant anthropogenic K^+ source to the middle Yellow River. A groundwater sample had a $\delta^{41}K$ value of -0.05 ± 0.00‰, which is comparable to the annual-average $\delta^{41}K_{rw}$ values in the middle Yellow River.

DISCUSSION

The export of K as solids in suspension (K_{SPM}) dominates the overall K flux in the middle Yellow River, averaging ~60% though time (Fig. S4). The highest proportion of K transport via solids occurs in the monsoon season, at typically ~95% and peaking at 99.7%. During the ice-melting interval, the proportion of K transported as solids also increase to ~95% (Fig. S4). The temporal patterns in the proportion of K exported as solids and in the total SPM concentration are similar to the pattern of seasonal variations in the $\delta^{41}K_{rw}$ values (Fig. S5), suggesting that the K isotopic behavior is closely related to the SPM content, via adsorption and/or incorporation processes.

Mass-balance calculations (see Supplementary Information) show that the weighted average silicate dissolution dominates the riverine K^+ budget (73.3 ± 6.3%), while evaporite dissolution contributes limited K^+ (25.8 ± 6.3%) to the middle Yellow River (Fig. 2). In contrast, although the K^+ contents of the carbonate leachates of the loess seem to be higher than expected for a pure carbonate and may inevitably also contain a non-carbonate K signal (Table S3), carbonate dissolution (0.06 ± 0.02% as an upper limit), atmospheric input (0.90 ± 0.10%), and anthropogenic input (0.03 ± 0.01%) play a negligible role in the riverine K^+ budget in the middle Yellow River (Fig. 2). These findings for the elemental budget are supported by the large difference between the $\delta^{41}K_{rw}$ values and the $\delta^{41}K$ values of both rain and anthropogenic input (Table S2). The 25.8 ± 6.3% input of K^+ from evaporites is comparable to its contribution to the dissolved Li^+ budget in this river[20]. The lack of a relationship between the proportions of K^+ from any sources (i.e. silicates, carbonates, and evaporites) and $\delta^{41}K_{rw}$ values rules out a dominant control on the $\delta^{41}K_{rw}$ variability by mixing between those sources (Fig. S6). Although atmospheric K^+ inputs (e.g., biomass burning, traffic emissions) are not significant in this basin, they may be relevant in other systems with higher atmospheric deposition, which would thus merit further investigation. Overall, silicate dissolution dominates the riverine K^+ budget, and the riverine K^+ flux is positively correlated with the PER (Fig. S2), both of which represent the preconditions for using K isotopes as a tracer for silicate weathering[8, 16].

Fertilizers are excluded as a contributor to the K^+ budget of the middle Yellow River, due to the sparse farmland and very negative $\delta^{41}K$ values of a sample from farmland (Table S2). Plant uptake can favor both light or heavy K isotopes[31], but we exclude the possibility of a vegetation control on $\delta^{41}K_{rw}$ in the middle Yellow River for three reasons. First, vegetation is very sparse in the (semi-)arid middle Yellow River[32]. Second, plant growth is enhanced after the ice-melting period, but the most negative $\delta^{41}K_{rw}$ values occur at this time yet, while there are similar $\delta^{41}K_{rw}$ values during both the ice-melting interval and the monsoon season (Fig.1). Third, plant defoliation should contribute a large amount of K^+ into the basin, but the K/Sr ratio smoothly decreased after August (Fig. S7). In contrast, the $\delta^{41}K_{rw}$ values are positively correlated with the K^+ flux and the chemical weathering rate (Fig. S8), suggesting a silicate weathering control on the K^+ budget, because evaporite-sourced K^+ should only be sensitive to water discharge rather than to chemical weathering rate. Together with the absence of source mixing relationships (Fig. S6) and the negligible carbonate-sourced K^+ (Fig. 2), the $\delta^{41}K_{rw}$ should predominantly reflect natural weathering processes, i.e. K^+ release from silicates and K^+ uptake by SPM[7, 8, 16] (Fig. S5).

The initial dissolution of K from rocks could kinetically release light K isotopes into the fluid, while the fractionation factor (α) during dissolution seems to be insensitive to mineralogy[33]. However, K isotopes have been shown to reach equilibrium after ~10 hours in laboratory experiments[33], whereas the interaction timescale between fluids and rocks in large watersheds ranges from seconds to years and is likely often in a disequilibrium state[34]. Therefore, K isotope fractionation during dissolution should be considered as a possibility. Here we employed both Rayleigh and batch models to simulate the dissolution processes for short and long timescales (Fig. 3). Such modelling only considers thermodynamic equilibrium and not any kinetic processes potentially affecting K partitioning between solid and aqueous phases.

The combined dissolution and incorporation process is modelled by assuming a constant α between fluid and SPM during each of the dissolution and subsequent incorporation processes (Fig. 3). The $\alpha_{SPM\text{-}fluid}$ for dissolution is obtained from published dissolution experiments, ranging between 1.00045 and 1.00105[36]. We further expand the range from 1.00000 to 1.00105[36] to cover a wider set of possibilities, because the above experiment was carried out in acidic conditions that may not be representative of the Yellow River[36].

The Rayleigh fractionation equation can be written as $\delta^{41}K_{rw} = (\delta^{41}K_{loess} + 1000)f^{(\alpha-1)} - 1000$, where $\delta^{41}K_{rw}$ and $\delta^{41}K_{loess}$ are the K isotopic compositions of the river water and loess, respectively, and *f* is the fraction of K remaining in the river water normalized to Na*, calculated from $[K/Na^*]_{rw}/[K/Na]_{loess}$[35] (here Na* = $[Na^+] - [Cl^-]$ to eliminate the impact of evaporite-sourced Na^+; Fig. 3). The α value for dissolution seems to be insensitive to mineralogy[34], but it varies during incorporation due to the variable site-preference of K^+. However, there is no α value available from silicate synthesis experiments so far, so we used $\alpha_{SPM\text{-}fluid} = (^{41}K/^{39}K)_{clay}/(^{41}K/^{39}K)_{rw}$ in a range between 0.99955 and 0.99895 obtained from our data (Table S1 for water and Fig. S3 for clays). These α values are broadly in the range of the 0.99976 deduced from *ab initio* calculations for equilibrium fractionation between fluids and illite[36] and 0.99937 and 0.99800-1.00000 estimated from various natural observations[12, 37].

Although the above selection of α values involves some uncertainties, the modelled trends cover our observations regardless of the exact choice of α values (Fig. 3). Simple incorporation of K^+ seems unable to explain the dataset, both because a source for dissolved K^+ is required and because the theoretically-calculated K/Na* ratios would be too high (for a given $\delta^{41}K_{rw}$ value) compared to the observed values (Fig. 3). However, mixing between the signatures of Rayleigh and/or batch dissolution, which release light K isotopes, and incorporation, which fractionates river water towards heavy K isotopes, could then explain the observations (Fig. 3).

A control of mass-dependent diffusion across the rock–fluid interface on K isotope variations in the Yellow River can be ruled out directly. For K^+ in water, the diffusion coefficient follows $D \propto m^{-\beta}$, with $0 \leq \beta < 0.20$[38], where D, m, and β refer to the diffusion coefficient, the mass of the diffusing particle, and the mass-scaling exponent, respectively. This relationship means that heavier or lighter ions would diffuse at slightly different rates. At the molecular level, this feature should affect how long water molecules stay in the first solvation shell around dissolved ions. If diffusion were important, then during the dry season (i.e. when river mixing is weaker), we would expect stronger isotope fractionation, leading to heavier Li and K isotopes in the water. However, the opposite trend is observed for K isotopes (Fig. 3). In addition, we observed a thermodynamic temperature control on seasonal variations in Li isotopes in the Yellow River[20], and since there is no correlation between Li and K isotopes, we rule out any dominant temperature effect on the K isotopes (Fig. S9).

Since the $\delta^{41}K_{rw}$ values are positively correlated with SPM concentrations (Fig. S5), and SPM mainly derives from erosion and aluminosilicate neoformation (Fig. S2), we also consider the potential for K isotope fractionation due to incorporation and/or adsorption processes after K release into fluids. However, we exclude adsorption as a main factor for two reasons. First, by analogy with evidence from nuclear magnetic resonance (NMR) spectroscopy on Li behavior, outer-sphere K is suggested to be fully hydrated and less isotopically fractionated relative to the source fluid[39], whereas experiments show that K adsorption preferentially removes heavy K isotopes onto surficial minerals[40]. However, we observe high $\delta^{41}K_{rw}$ at times with high SPM concentrations (Fig. S5), implying removal of light K isotopes, which could not be explained by such adsorption processes. Second, Ba isotopes suggest Ba^{2+} removal via adsorption, whereas K and Ba isotopes show no relationship (Fig. S10). In contrast, incorporation into clays favors light K^+ although interlayer K could get fully hydrated and be less fractionated relative to the source fluid[9], which is supported by *ab initio* calculations[36] and natural observations[12, 37].

Overall, the processes of silicate dissolution followed by incorporation into clays appear to dominate the $\delta^{41}K_{rw}$ variability. A control on $\delta^{41}K_{rw}$ by clay formation is also supported by the co-variation between dissolved K/Na* and Si/Na* ratios (Fig. S11), which could be explained by simultaneous removal of Si and K^+ during aluminosilicate neoformation. Furthermore, we calculated the saturation indices (SI) of various minerals in the sampled waters using PHREEQC (version 3; Table S4)[41], considering parameters including pH, water temperature, Ca^{2+}, K^+, Mg^{2+}, Na^+, F^-, Cl^-, NO_3^-, SO_4^{2-}, CO_3^{2-}, Si, Sr^{2+}, Ba^{2+}, Al, Fe, and Mn concentrations. Saturation indices > 0 calculated by PHREEQC for some K-bearing aluminosilicates (Table S4)[41], together with the reported illite neoformation in microenvironments (despite overall undersaturation)[42], support that clay formation could be the main driver of $\delta^{41}K_{rw}$.

The SPM in rivers mainly results from physical erosion and aluminosilicate neoformation[5], whereas dissolved K^+ in rivers is derived from silicate dissolution

(Fig. 2). Riverine $\delta^{41}K_{rw}$ values are dominated by the isotopic fractionation during incorporation following dissolution (Fig. 3). Therefore, a high ratio between the dissolved K^+ flux and the solid K flux transported via SPM reflects a high silicate weathering intensity (i.e. most K is dissolved), and corresponds to low $\delta^{41}K_{rw}$ values due to solid dissolution (Figs. 4 and 5). In contrast, a low ratio between the dissolved K^+ flux and the solid K flux transported via SPM reflects a low silicate weathering intensity (i.e. most K is in solid), and corresponds to high $\delta^{41}K_{rw}$ values due to light K^+ removal into clays (Figs. 4 and 5). A control through this process of aluminosilicate neoformation is also supported by a broad negative co-variation of $\delta^{41}K_{rw}$ values with$\delta^{26}Mg_{rw}$ data (Fig. S12)[18]. Although K^+ is mainly sourced from silicate dissolution, there is a non-negligible evaporite input in the middle Yellow River, so that we use W/D to reflect silicate weathering intensity, where W is the silicate chemical weathering flux and D is the total denudation[21] (Fig. 5). As such, $\delta^{41}K_{rw}$ values are expected to negatively correlate with W/D changes through time[7], as observed, from which we derive an empirical correlation of $\delta^{41}K_{rw} = -0.07 \times \ln(W/D) - 0.38$ (Fig. 5). Unlike riverine Li isotopes which are also proposed to reflect silicate weathering intensity due to fractionation during incorporation into secondary minerals, but with a "boomerang" pattern[43], K isotopes show a unidirectional pattern with W/D (Fig. 5), which may be beneficial in facilitating the application of $\delta^{41}K_{rw}$ as a tracer of silicate weathering intensity.

Considering that $\delta^{41}K_{rw}$ values reflect an instantaneous snapshot between silicate dissolution and aluminosilicate neoformation, with strong seasonality, the longer-term (e.g. annually-averaged) W/D may not be expected to co-vary with instantaneous spot-sampled $\delta^{41}K_{rw}$ values in a spatial sampling strategy[8]. Nevertheless, it is interesting to note that the $\delta^{41}K_{rw}$ data reported from global rivers seem overall lower than our observed values, and even lower than the UCC for a few samples (Fig. 5), which requires further investigation. However, we suggest this discrepancy could be attributable to three factors: (1) some of the spatial samples were filtered with a 0.45 μm filter that could potentially contain more colloidal material comprising neo-formed aluminosilicates with light incorporated K isotopes[8] (see clay values in Fig. S3); and/or (2) unacidified samples may have been susceptible to contamination by biota; and/or (3) the calculated weathering intensity (W/D) based on sampling several decades ago could have changed significantly in recent years (e.g. the Yellow River has only a 20% SPM yield today compared to half a century ago[22, 44]). In combination, we contend that the relationship between W/D ratios and $\delta^{41}K_{rw}$ values has typically been obscured in spatial investigations[8, 16], whereas the high-resolution time series sampling strategy used here, and which captured a once in a century storm event, demonstrates that $\delta^{41}K_{rw}$ values negatively correlate with W/D ratios. Hence, $\delta^{41}K_{rw}$ values provide a novel tool for assessing silicate weathering intensity. However, we would encourage further research on a wider range of modern river systems to better validate this empirical relationship, and to reveal any environmental circumstances in which it might be significantly altered or break down.

Global seawater ($\delta^{41}K_{sw}$ ~+0.12 ‰)[45] is significantly isotopically heavier than the UCC ($\delta^{41}K$ ~-0.44 ‰)[11], which has mainly been attributed to K^+ removal through sediment sinks, early diagenesis, oceanic crust alteration, and reverse weathering[12, 45-48]. In contrast, K^+ release from mid-ocean ridge vent systems is limited and also has low $\delta^{41}K$ values (-0.46‰ or -0.15‰)[37]. The reported average terrestrial weathering input of K isotopes ($\delta^{41}K = -0.38 \pm 0.04$‰)[8] is also low, but constraints on seasonal variability have been lacking until now[7, 8]. Here we show that $\delta^{41}K_{rw}$ could vary significantly on seasonal timescales and can reach values as high as +0.27‰ under extreme incongruent weathering conditions (W/D<0.0001, Fig. 5) in which large amounts of nucleation help to drive aluminosilicate neoformation. Our findings indicate that major temporal $\delta^{41}K_{rw}$ variations in riverine inputs, possibly arising from Tibetan Plateau uplift and other orogenic events during the Cenozoic, could potentially explain the $\delta^{41}K_{sw}$ evolution without any other processes[12, 45-48].

In deep time, the weathering of the UCC can be conceptualized as a globally integrated source of dissolved K^+ to the oceans. As such, the variability in marine K isotopic compositions preserved in sedimentary archives may reflect silicate weathering intensity on the Earth through time. Since carbonates are vulnerable to biological fractionation of K isotopes[49], oceanic authigenic clay minerals (e.g. illite, glauconite, Fe-smectite) with a more constant (albeit likely temperature-dependent) fractionation factor from seawater could potentially serve as a robust archive of paleo-seawater K isotopes. Such records could enable the effective reconstruction of long-term changes in Earth's weathering-climate feedback[1-3].

METHODS

Information on the field sampling, extraction experiment on the loess, geochemical analyses, and K isotope analyses is described below.

Field sampling

A total of 60 river water samples were collected weekly in 2013 at the Longmen hydrological station (35°40′06.43″ N; 110°35′22.88″ E; Table S1). This station is located in the middle reaches of the Yellow River, after the convergence of most tributaries draining the Chinese Loess Plateau (Fig. S1). Note that four river water samples (LM13-31 to 13-34) were collected daily during a storm event in July[18-21]. Three rain water samples were collected in July and August 2013 at the station to assess atmospheric inputs, and a sewage sample (TKT1) and a groundwater sample (T10GW) were collected in farmland adjacent to the station to constrain the composition of anthropogenic and groundwater K inputs[18-21] (Table S2).

All river water samples were collected 0.5 m below the river surface in the central part of the river channel. For each sample, water temperature, pH, electrical conductivity (EC), and total dissolved solids (TDS) were measured *in situ*. All water samples were filtered through 0.2 μm nylon filters on site. Filtered water samples were stored in pre-cleaned polyethylene bottles, acidified to pH <2 with distilled HNO_3, and stored at 4°C, before analysis of major cationic concentrations and K isotopes.

Sequential extraction experiment for loess

Five fresh loess samples were collected from five typical layers of the loess profile at Lingtai and were subjected to sequential extraction for K isotopes (Table S3). Briefly, 0.5 g of milled loess was leached with 18.2 MΩ.cm water for 5 minutes, and centrifuged and filtered via manual filters to collect the water-soluble fraction[21]. The residue was then leached for 2 h with 5% acetic acid (HAc) at 75 °C, and then centrifuged to collect the carbonate fraction[23, 24]. The residues of the leaching procedure were digested with HF–HCl–HNO_3 to constrain the silicate fraction.

Geochemical analyses

The concentrations of major ions for all samples were reported by Zhang et al. (2015)[21]. Major cations (including K^+) were analyzed by a Leeman Labs Profile inductively coupled plasma atomic emission spectroscopy (ICP-AES), with a relative standard deviation (RSD) better than 5% according to in-house standards and reference materials. Major anions (F^-, Cl^-, and SO_4^{2-}) were measured by ion chromatography (ICS 1200) and NO_3^- was measured by a Skalar continuous flow analyzer, with an RSD better than 5%. Alkalinity (expressed as HCO_3^-) was measured by a Shimadzu Corporation total organic carbon analyzer (TOC-V_{CPH}), with an RSD better than 5%. The percent charge balance error (CBE), as a measure of the data quality, is given by the equation [CBE (%) = $(TZ^+ - TZ^-)/(TZ^+ + TZ^-) \times 100$], where $TZ^+ = 2Ca^{2+} + 2Mg^{2+} + K^+ + Na^+$, $TZ^- = Cl^- + 2SO_4^{2-} + NO_3^- + HCO_3^-$, with an average better than ± 5%.

K isotope analyses

Pre-treatment and analyses of the K isotopic compositions of all samples of river water, rain water, sewage water, and groundwater were performed in an ultraclean room (class 1000) at the Hefei University of Technology (HFUT)[49]. Typically, 2 mL of river water, sewage water, and groundwater, and ~20 mL of rain water were used, enabling 1 μg K^+ to be retrieved. These samples were dried down after organic matter digestion (using 1 mL of concentrated H_2O_2 and HNO_3), and then re-dissolved in 0.5 M HNO_3, before K purification by column chromatography. The samples were passed twice through Savillex® PFA microcolumns (0.64 cm × 8 cm, inner diameter and length, respectively) filled with 2 mL resin (Bio-Rad® AG50W X-8, 200-400 mesh) for cation exchange chromatography, with 0.5 M HNO_3 as eluent[50]. The columns were pre-cleaned with 12 mL of an acid mixture of 6 M HNO_3 + 0.5 M HF. The purified K fraction was re-dissolved in 2% HNO_3 and diluted in order to obtain 200 μg/L of K for K isotope measurements. The total procedural blank of this method was less than 10 ng K, which is negligible relative to 1 μg of K analyzed in each sample[50].

Isotopic analyses were conducted on a *Neptune Plus* multi-collector inductively coupled plasma mass spectrometer (MC-ICP-MS, Thermo Fisher, Germany) at the HFUT. Analyses used a "Continuous-Acquisition-Method" and sample-standard-bracketing (SSB) with the international standard NIST SRM999c for instrumental mass fractionation correction[50]. The K isotopic composition ($\delta^{41}K$) is reported using the delta-notation in per mil:

$$\delta^{41}K\ (‰) = \left(\frac{\frac{^{41}K}{^{39}K}(\mathrm{sample})}{\frac{^{41}K}{^{39}K}(\mathrm{SRM999c})} - 1\right) \times 1000‰ \qquad \text{Eq. (1)}$$

where SRM999c is the average value of the standard solution measured immediately before and after each sample. Note that some previous data were reported relative to different standards, i.e. SRM3141a, SRM918b, and SRM193[51-53]. All standards were demonstrated to be indistinguishable for their $\delta^{41}K$, within current analytical precision[50]. The $\delta^{41}K$ value was obtained from triplicate measurements, from which mean values and the standard deviation (2 s.d.) were calculated for each sample.

In order to validate the measured K isotope data, four in-house standards (GBW-K, GSB-K, QC-K, and ST-K) were analyzed repeatedly and yielded $\delta^{41}K$ values of 0.29 ± 0.10‰ (2 s.d., n = 5), 0.31 ± 0.12‰ (2 s.d., n = 5), 0.25 ± 0.06‰ (2 s.d., n = 2), and -0.07 ± 0.03‰ (2 s.d., n = 5), respectively, in agreement with previous measured values at the HFUT[50]. Moreover, K from a seawater standard (NASS-5) and two rock reference materials (AGV-2, BHVO-2) was purified following this procedure, giving $\delta^{41}K_{NASS-5}$ of +0.13 ± 0.08‰ (2 s.d., n = 4), $\delta^{41}K_{AGV-2}$ of -0.44 ± 0.11‰ (2 s.d., n = 7), and $\delta^{41}K_{BHVO-2}$ of -0.52 ± 0.04‰ (2 s.d., n = 2), in line with previously published data[50-53]. Overall, the long-term external reproducibility is better than 0.11‰ (2 s.d.) for $\delta^{41}K$ measurements[50].

Data availability. The datasets generated in this study are provided in the supplementary Information. Source Data is provided with this paper https://doi.org/10.6084/m9.figshare.30665387.

Code availability statement: The code used in this manuscript (PHREEQC software) is available for download from the U.S. Geological Survey website: https://www.usgs.gov/software/phreeqc-version-3.

References

1. Walker JCG, Hays PB, Kasting JF. A negative feedback mechanism for the long-term stabilization of Earth's surface temperature. *Journal of Geophysical Research: Oceans* **86**, 9776-9782 (1981).

2. Berner RA, Lasaga AC, Garrels RM. The carbonate-silicate geochemical cycle and its effect on atmospheric carbon-dioxide over the Past 100 Million years. *American Journal of Science* **283**, 641-683 (1983).

3. Hilton RG, West AJ. Mountains, erosion and the carbon cycle. *Nature Reviews Earth & Environment* **1**, 284-299 (2020).

4. Raymo ME, Ruddiman WF. Tectonic forcing of late Cenozoic climate. *Nature* **359**, 117-122 (1992).

5. Gaillardet J, Dupre B, Louvat P, Allegre CJ. Global silicate weathering and CO_2 consumption rates deduced from the chemistry of large rivers. *Chemical Geology* **159**, 3-30 (1999).

6. West AJ, Galy A, Bickle M. Tectonic and climatic controls on silicate weathering. *Earth and Planetary Science Letters* **235**, 211-228 (2005).

7. Li S, Li W, Raymo ME, Wang X, Chen Y, Chen J. K isotopes as a tracer for continental weathering and geological K cycling. *Proceedings of the National Academy of Sciences of the United States of America* **116**, 8740-8745 (2019).

8. Wang K, Peucker-Ehrenbrink B, Chen H, Lee H, Hasenmueller EA. Dissolved potassium isotopic composition of major world rivers. *Geochimica et Cosmochim Acta* **294**, 145-159 (2021).

9. Teng F-Z, Hu Y, Ma J-L, Wei G-J, Rudnick RL. Potassium isotope fractionation during continental weathering and implications for global K isotopic balance. *Geochimica et Cosmochimica Acta* **278**, 261-271 (2020).

10. Chen H, Liu X-M, Wang K. Potassium isotope fractionation during chemical weathering of basalts. *Earth and Planetary Science Letters* **539**, 116192 (2020).

11. Huang T-Y, Teng F-Z, Rudnick LR, Chen X-Y, Hu Y, Liu YS, Wu F-Y. Heterogeneous potassium isotopic composition of the upper continental crust. *Geochimica et Cosmochimica Acta* **278**, 122-136 (2020).

12. Santiago Ramos DP, Morgan LE, Lloyd NS, Higgins JA. Reverse weathering in marine sediments and the geochemical cycle of potassium in seawater: Insights from the K isotopic composition ($^{41}K/^{39}K$) of deep-sea pore-fluids. *Geochimica et Cosmochimica Acta* **236**, 99-120 (2018).

13. Deng K, Yang S, Guo Y. A global temperature control of silicate weathering intensity. *Nature Communications* **13**, 1781 (2022).

14. Brantley SL, Shaughnessy A, Lebedeva MI, Balashov VN. How temperature-dependent silicate weathering acts as Earth's geological thermostat. *Science* **379**, 382-389 (2023).

15. Lasaga AC. Rate laws of chemical reactions. *Reviews in Mineralogy and Geochemistry* **8**, 1-66 (1981).

16. Li X, Han G, Liu M, Liu J, Zhang Q, Qu R. Potassium and its isotope behaviour during chemical weathering in a tropical catchment affected by evaporite dissolution. *Geochimica et Cosmochimica Acta* **316**, 105-121 (2022).

17. Taylor SR, McLennan SM, McCulloch MT. Geochemistry of loess, continental crustal composition and crustal model ages. *Geochimica et Cosmochimica Acta* **47**, 1897-1905 (1983).

18. Gou L-F, Jin Z, Galy A, Xu Y, Xiao J, Yang Y, Bouchez J, Pogge von Strandmann PAE, Jin C, Yang S, Zhao Z-Q. Seasonal Mg isotopic variation in the middle Yellow River: Sources and fractionation. *Chemical Geology* **619**, 121314 (2023).

19. Gou L-F, Jin Z, Galy A, Gong Y-Z, Nan X-Y, Jin C, Wang X-D, Bouchez J, Cai H-

M, Chen J-B, Yu H-M, Huang F. Seasonal riverine barium isotopic variation in the middle Yellow River: Sources and fractionation. *Earth and Planetary Science Letters* **531**, 115990 (2020).

20. Gou L-F, Jin Z, Pogge von Strandmann PAE, Li G, Qu Y-X, Xiao J, Deng L, Galy A. Lithium isotopes in the middle Yellow River: Seasonal variability, sources and fractionation. *Geochemica et Cosmochemica Acta* **248**, 88-108 (2019).

21. Zhang Q, Jin Z, Zhang F, Xiao J. Seasonal variation in river water chemistry of the middle reaches of the Yellow River and its controlling factors. *Journal of Geochemical Exploration* **156**, 101-113 (2015).

22. Saito Y, Yang ZS, Hori K. The Huanghe (Yellow River) and Changjiang (Yangtze River) deltas: A review on their characteristics, evolution and sediment discharge during the Holocene. *Geomorphology* **41**, 219-231 (2001).

23. Yokoo Y, Nakano T, Nishikawa M, Quan H. Mineralogical variation of Sr–Nd isotopic and elemental compositions in loess and desert sand from the central Loess Plateau in China as a provenance tracer of wet and dry deposition in the northwestern Pacific. *Chemical Geology* **204**, 45-62 (2004).

24. Tessier A, Campbell PGC, Bisson M. Sequential extraction procedure for the speciation of particulate trace-metals. *Analytical Chemistry* **51**, 844-851 (1979).

25. Li YH, Teraoka H, Yang TS, Chen JS. The elemental composition of suspended particles from the Yellow and Yangtze Rivers. *Geochimica et Cosmochimica Acta* **48**, 1561-1564 (1984).

26. Murphy DM, Froyd KD, Bian H, Brock CA, Dibb JE, DiGangi JP, Diskin G, Dollner M, Kupc A, Scheuer E, Schill GP, Weinzierl B, Williamson CJ, Yu P. The distribution of sea-salt aerosol in the global troposphere. *Atmospheric Chemistry and Physics* **19**, 4093-4104 (2019).

27. Jin Z, You C-F, Yu J, Wu L, Zhang F, Liu H-C. Seasonal contributions of catchment weathering and eolian dust to river water chemistry, northeastern Tibetan Plateau: Chemical and Sr isotopic constraints. *Journal of Geophysical Research: Earth Surface* **116**, F04006 (2011).

28. Wang K, Jacobsen SB. An estimate of the Bulk Silicate Earth potassium isotopic composition based on MC-ICPMS measurements of basalts. *Geochimica et Cosmochimica Acta* **178**, 223-232 (2016).

29. Li W, Kwon KD, Li S, Beard BL. Potassium isotope fractionation between K-salts and saturated aqueous solutions at room temperature: Laboratory experiments

and theoretical calculations. *Geochimica et Cosmochimica Acta* **214**, 1-13 (2017).

30. Schauble EA. Applying stable isotope fractionation theory to new systems. *Reviews in Mineralogy and Geochemistry* **55**, 65-111 (2004).

31. Christensen JN, Qin L, Brown ST, DePaolo DJ. Potassium and calcium isotopic fractionation by plants (Soybean [*Glycine max*], Rice [*Oryza sativa*], and Wheat [*Triticum aestivum*]). *ACS Earth and Space Chemistry* **2**, 745-752 (2018).

32. Chen J, Wang F, Meybeck M, He D, Xia X, Zhang L. Spatial and temporal analysis of water chemistry records (1958-2000) in the Huanghe (Yellow River) basin. *Global Biogeochemical Cycles* **19**, GB3016 (2005).

33. Li W, Liu X-M, Wang K, Koefoed P. Lithium and potassium isotope fractionation during silicate rock dissolution: An experimental approach. *Chemical Geology* **568**, 120142 (2021).

34. Maher K. The dependence of chemical weathering rates on fluid residence time. *Earth and Planetary Science Letters* **294**, 101-110 (2010).

35. Sauzeat L, Rudnick RL, Chauvel C, Garcon M, Tang M. New perspectives on the Li isotopic composition of the upper continental crust and its weathering signature. *Earth and Planetary Science Letters* **428**, 181-192 (2015).

36. Zeng H, Rozsa VF, Nie NX, Zhang Z, Pham TA, Galli G, Dauphas N. *Ab initio* calculation of equilibrium isotopic fractionations of potassium and rubidium in minerals and water. *ACS Earth and Space Chemistry* **3**, 2601-2612 (2019).

37. Zheng X-Y, Beard BL, Neuman M, Fahnestock MF, Bryce JG, Johnson CM. Stable potassium (K) isotope characteristics at mid-ocean ridge hydrothermal vents and its implications for the global K cycle. *Earth and Planetary Science Letters* **593**, 117653 (2022).

38. Bourg IC, Richter FM, Christensen JN, Sposito G. Isotopic mass dependence of metal cation diffusion coefficients in liquid water. *Geochimica et Cosmochimica Acta* **74**, 2249-2256 (2010).

39. Hindshaw RS, Tosca R, Gout TL, Farnan I, Tosca NJ, Tipper ET. Experimental constraints on Li isotope fractionation during clay formation. *Geochimica et Cosmochimica Acta* **250**, 219-237 (2019).

40. Li W, Liu X-M, Hu Y, Teng F-Z, Hu Y. Potassium isotopic fractionation during clay adsorption. *Geochimica et Cosmochimica Acta* **304**, 160-177 (2021).

41. Parkhurst D, Appelo CAJ. User's guide to PHREEQC (Version 2): A computer program for speciation, batch-reaction, one-dimensional transport, and inverse geochemical calculations. In: *Water-Resources Investigations Report* (1999).

42. Lu M, Diao Q-F, Zheng Y-Y, Yin Z-Y, Dai Z. Influence of water on tensile behavior of illite through the molecular dynamics method. *International Journal of Geomechanics* **24**, 04024024 (2024).

43. Dellinger M, Gaillardet J, Bouchez J, Calmels D, Louvat P, Dosseto A, Gorge C, Alanoca L, Maurice L. Riverine Li isotope fractionation in the Amazon River basin controlled by the weathering regimes. *Geochimica et Cosmochimica Acta* **164**, 71-93 (2015).

44. Zhang J, Huang WW, Letolle R, Jusserand C. Major-element chemistry of the Huanghe (Yellow-river), China - Weathering processes and chemical fluxes. *Journal of Hydrology* **168**, 173-203 (1995).

45. Wang K, Close HG, Tuller-Ross B, Chen H. Global average potassium isotope composition of modern seawater. *ACS Earth and Space Chemistry* **4**, 1010-1017 (2020).

46. Li W, Liu X-M, Wang K, McManus J, Haley BA, Takahashi Y, Shakouri M, Hu Y. Potassium isotope signatures in modern marine sediments: Insights into early diagenesis. *Earth and Planetary Science Letters* **599**, 117849 (2022).

47. Santiago Ramos DP, Nielsen SG, Coogan LA, Scheuermann PP, Seyfried WE, Higgins JA. The effect of high-temperature alteration of oceanic crust on the potassium isotopic composition of seawater. *Geochimica et Cosmochimica Acta* **339**, 1-11 (2022).

48. Santiago Ramos DP, Coogan LA, Murphy JG, Higgins JA. Low-temperature oceanic crust alteration and the isotopic budgets of potassium and magnesium in seawater. *Earth and Planetary Science Letters* **541**, 116290 (2020).

49. Li W, Liu X-M, Wang K, Hu Y, Suzuki A, Yoshimura T. Potassium incorporation and isotope fractionation in cultured scleractinian corals. *Earth and Planetary Science Letters* **581**, 117393 (2022).

50. Huang C, Gu H-O, Sun H, Wang F, Chen B. High-precision determination of stable potassium and magnesium isotopes utilizing single column separation and multicollector inductively coupled plasma mass spectrometry. *Spectrochimica Acta Part B: Atomic Spectroscopy* **181**, 106232 (2021).

51. Hu Y, Teng F-Z, Plank T, Chauvel C. Potassium isotopic heterogeneity in

subducting oceanic plates. *Science Advances* **6**, eabb2472 (2020).

52. Morgan LE, Santiago Ramos DP, Davidheiser-Kroll B, Faithfull J, Lloyd NS, Ellam RM, Higgins JA. High-precision $^{41}K/^{39}K$ measurements by MC-ICP-MS indicate terrestrial variability of $\delta^{41}K$. *Journal of Analytical Atomic Spectrometry* **33**, 175-186 (2018).

53. Chen H, Tian Z, Tuller-Ross B, Korotev RL, Wang K. High-precision potassium isotopic analysis by MC-ICP-MS: An inter-laboratory comparison and refined K atomic weight. *Journal of Analytical Atomic Spectrometry* **34**, 160-171 (2019).

Acknowledgements: This work was financially supported by NSFC (42221003 and 42530512 to Z. Jin; 42373054 to L.-F. Gou; and 42373001 to H. Sun), and ERC Consolidator grant 682760 to PPvS. DJW was supported by a Natural Environment Research Council independent research fellowship (NE/T011440/1). X.-Y. Zheng, S. Li, J. Wang, F. Zhang, and M. He are thanked for their insightful comments that benefited this manuscript. C. Huang at Hefei University of Technology is thanked for his help during laboratory work.

Author contributions

Z. Jin and L.-F. Gou conceived and led this project, designed and executed the experiments, and wrote the draft manuscript. P. Pogge von Strandmann, W. Li, D.J. Wilson, J. Xiao, Z.-Q. Zhao, and A. Galy discussed the results and reviewed the manuscript. H. Sun and H. Gu analyzed the samples and discussed the results.

Competing interests: None.

Additional information

Supplementary Information accompanies this paper at https://doi.org/1....

Figure legends:

Figure 1 Seasonal hydrological and geochemical parameters for the middle Yellow River during 2013. (A) Cl^- concentration ($[Cl^-]$), (B) Na^+ concentration ($[Na^+]$), (C) K^+ concentration ($[K^+]$), and (D) $\delta^{41}K_{rw}$ values of river water collected weekly at the Longmen hydrological station. (G) Ratios between SPM K flux and dissolved K^+ flux, (H) suspended particulate matter (SPM) flux, and (J) physical erosion rate (PER, from Zhang et al., 2015)[21] at the Longmen station. Also shown for comparison are (E) water temperatures (orange squares) and air temperatures (open blue squares), and (F) water discharge. The ice-melting interval (16th March to 13th April), monsoon season (June to mid-September), and a storm event (22nd to 25th July) are shaded green, pale blue, and dark blue, respectively.

Figure 2 Partitioning of the dissolved K^+ budget into five end-members, *i.e.* evaporites, rain, anthropogenic, carbonates, and silicates. The weathering of silicates dominates the dissolved K^+ budget (an annual average of 73 ± 6%), while another significant contributor is evaporites (26 ± 6%), whereas the other contributions are negligible. See supplementary text for the calculations.

Figure 3 $\delta^{41}K_{rw}$ versus K/Na* ratios, where Na* = $[Na^+]$ - $[Cl^-]$. The curves indicate modelled silicate dissolution (batch or Rayleigh fractionation) followed by aluminosilicate neoformation (Rayleigh fractionation), with potential fractionation factors based on Li et al. (2021)[33]. The loess K/Na* ratio is calculated from Sauzeat et al. (2015) and Huang et al. (2020)[11, 35]. The labeled bars show the proportion of remaining K^+ relative to the conservative Na^+ The pink and brown shadings show the feasible zones from Rayleigh and Batch dissolution, respectively..

Figure 4 Correlation of $\delta^{41}K_{rw}$ values with the ratio of the SPM K flux to the dissolved K flux (on a logarithmic scale).

Figure 5 Cross plot of spatial and temporal variations in $\delta^{41}K_{rw}$ versus silicate weathering intensity (W/D, where W = silicate weathering rate, D = denudation rate). Data are from the Yellow River (this study, 51 samples), Li et al. (2019)[7] for the Yangtze and other rivers, and Wang et al. (2021)[8] for global large rivers. The blue line is a regression between $\delta^{41}K_{rw}$ and W/D based on data for the Yellow and Yangtze rivers. The $\delta^{41}K_{rw}$ data from global large rivers are excluded from the regression because they represent snapshot sampling, which may not reflect the inter-annual average W/D conditions. Values for the $\delta^{41}K$ of seawater are from Wang et al. (2021)[8], and the Upper Continental Crust (UCC) and loess data are from Huang et al. (2020)[11].

Editor Summary:

Seasonal variation in K isotopes of rivers that drain the Chinese Loess Plateau indicates that riverine K isotopes can trace changes in silicate weathering intensity over time, offering a tool to track Earth's climate–rock interactions.

Peer Review Information:

Nature Communications thanks the anonymous reviewers for their contribution to the peer review of this work. A peer review file is available.

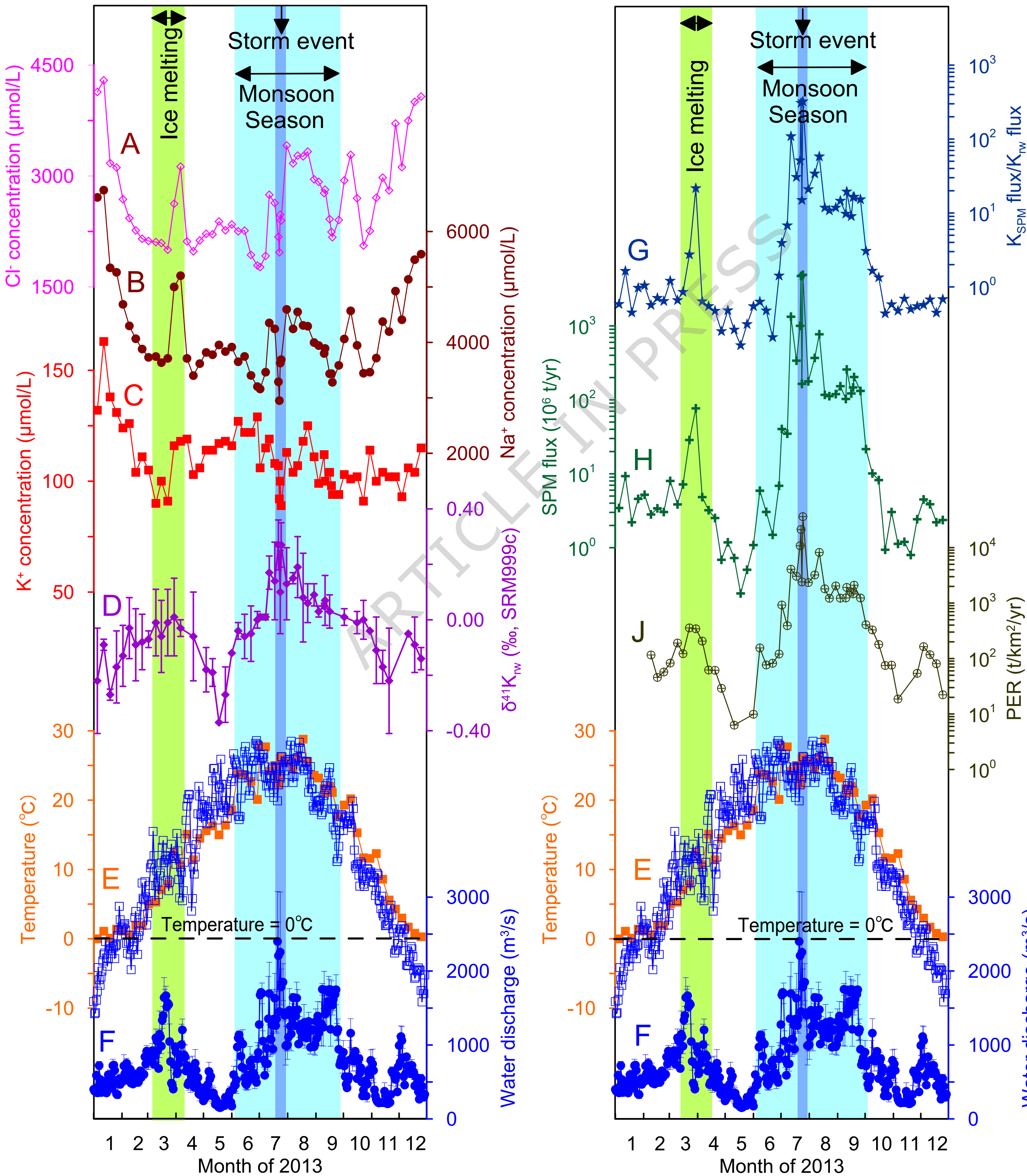
Ice melting
Storm event
Monsoon Season
A
B
C
D
E
F
G
H
J
Cl- concentration (μmol/L)
4500
3000
1500
Na+ concentration (μmol/L)
6000
4000
2000
K+ concentration (μmol/L)
150
100
50
δ41Krw (‰, SRM999c)
0.40
0.00
-0.40
Temperature (°C)
30
20
10
0
-10
Temperature = 0°C
Water discharge (m3/s)
3000
2000
1000
0
1 2 3 4 5 6 7 8 9 10 11 12
Month of 2013
KSPM flux/Krw flux
SPM flux (106 t/yr)
PER (t/km2/yr)

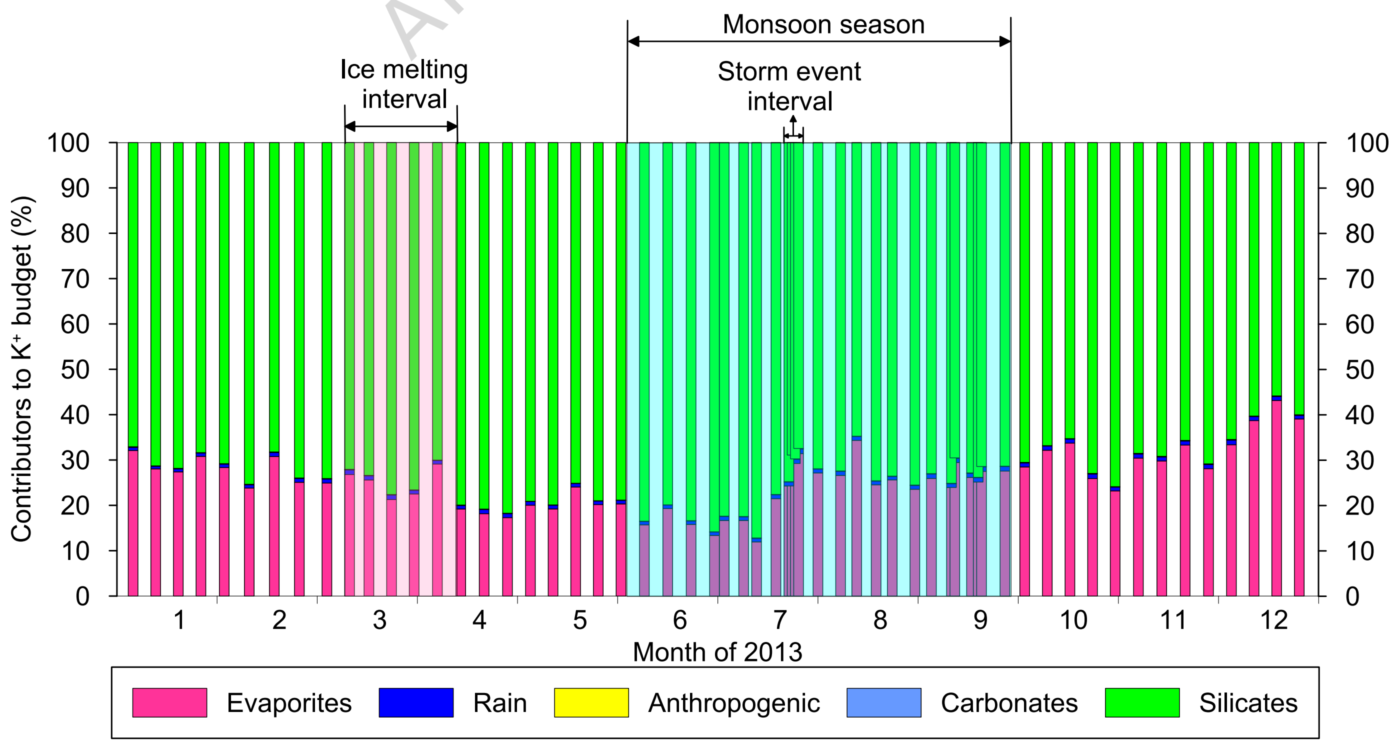

Monsoon season
Ice melting interval
Storm event interval
Contributors to K⁺ budget (%)
100
90
80
70
60
50
40
30
20
10
0
1
2
3
4
5
6
7
8
9
10
11
12
Month of 2013
Evaporites
Rain
Anthropogenic
Carbonates
Silicates

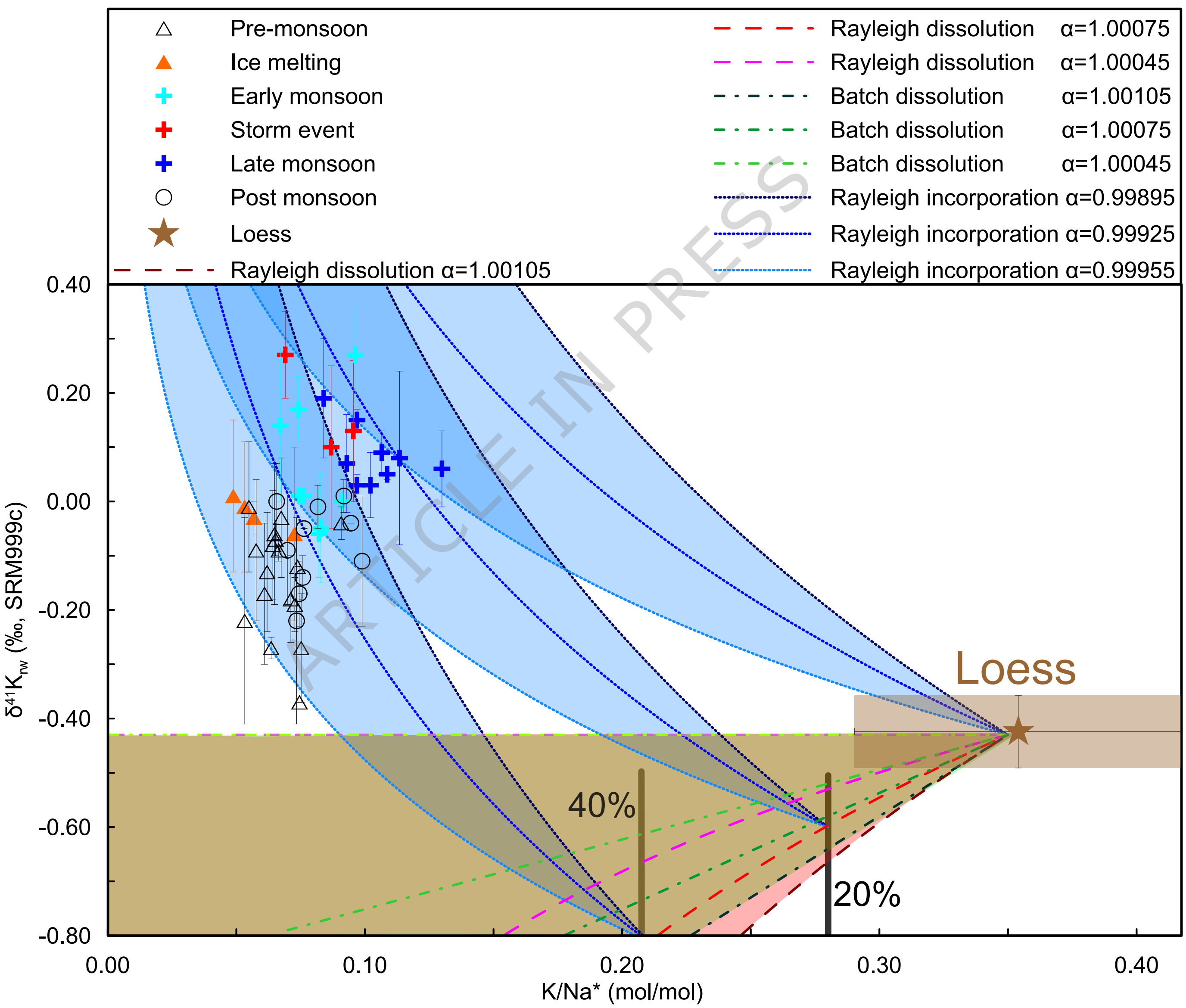
Pre-monsoon
Ice melting
Early monsoon
Storm event
Late monsoon
Post monsoon
Loess
Rayleigh dissolution α=1.00105
Rayleigh dissolution α=1.00075
Rayleigh dissolution α=1.00045
Batch dissolution α=1.00105
Batch dissolution α=1.00075
Batch dissolution α=1.00045
Rayleigh incorporation α=0.99895
Rayleigh incorporation α=0.99925
Rayleigh incorporation α=0.99955
Loess
40%
20%
δ41Krw (‰, SRM999c)
K/Na* (mol/mol)
0.40
0.20
0.00
-0.20
-0.40
-0.60
-0.80
0.00
0.10
0.20
0.30
0.40
ARTICLE IN PRESS

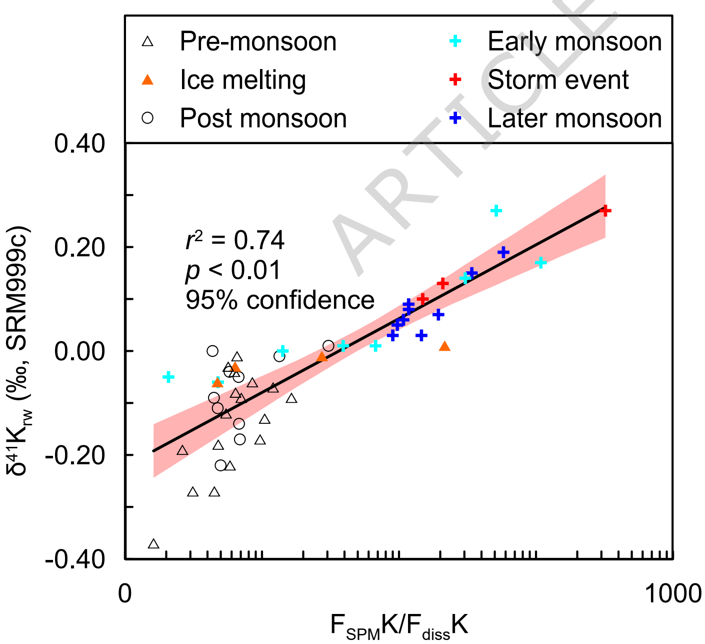

Pre-monsoon
Ice melting
Post monsoon
Early monsoon
Storm event
Later monsoon
r^2 = 0.74
p < 0.01
95% confidence
0.40
0.20
0.00
-0.20
-0.40
0
1000
$\delta^{41}K_{rw}$ (‰, SRM999c)
$F_{SPM}K/F_{diss}K$

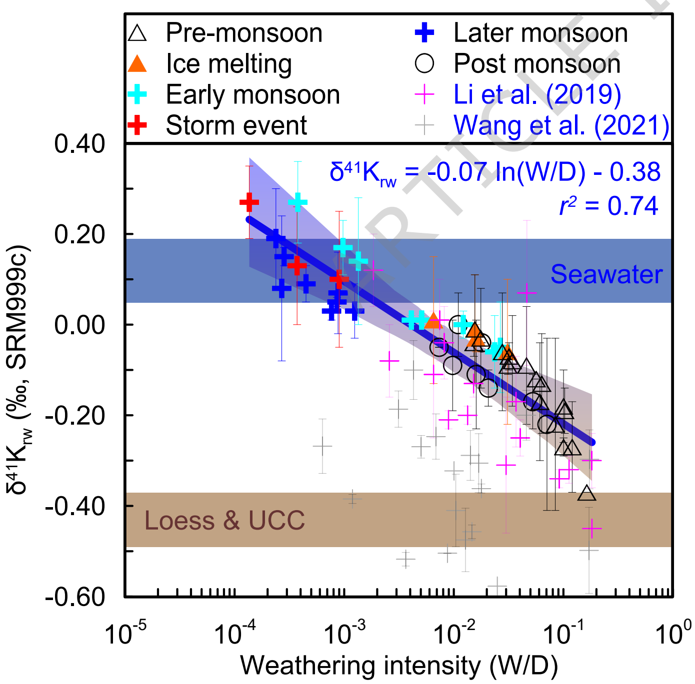
Pre-monsoon
Later monsoon
Ice melting
Post monsoon
Early monsoon
Li et al. (2019)
Storm event
Wang et al. (2021)
δ41Krw = -0.07 ln(W/D) - 0.38
r2 = 0.74
Seawater
Loess & UCC
0.40
0.20
0.00
-0.20
-0.40
-0.60
δ41Krw (‰, SRM999c)
10-5
10-4
10-3
10-2
10-1
100
Weathering intensity (W/D)